Chapter 2

Background

Unlike transient absorption spectroscopy TR-2PPE is not selective to transitions between molecular levels. In general it is not possible to distinguish between electrons photoemitted from a molecular level and isoenergetic electrons emitted from the conduction band of the substrate. Nevertheless, the probe depth is restricted by the penetration depth of the probe-light and the escape-depth of the photoelectrons. Thus, part of the 2PPE signal will originate from conduction band electrons.
In Sec. 2.1 the electron transfer process will be illustrated first within the classical Marcus model for homogeneous electron transfer and then extended to a quantum mechanical model. For heterogeneous electron transfer the relevant literature with the recently developed theoretical model is quoted. The relevance of the experimental data obtained in this work for the first time is pointed out for verification and comparison of the theory.
The dynamics of injected electrons are described in terms of an electron distribution in the band structure of the substrate and will be discussed in Sec. 2.2.
In Sec. 2.3 the interaction between the molecules and the substrate is discussed in terms of the alignment of the molecular levels in the ground state with respect to the band structure of the substrate .
Both aforementioned processes occur on time scales ranging down to a few femtoseconds or less. Section 2.5 deals with light pulses as short as 15 fs and related phenomena.
A general description of the experimental systems investigated in this work is given in Sec.2.6.
An overview of the time-resolved two-photon photoemission technique (TR-2PPE) is given in Sec. 2.4.

2.1 Electron transfer

Electron transfer (ET) is one of the most fundamental chemical processes of far reaching importance for biology, chemistry and physics. 50 years of intense investigations by chemists and physicists brought a deep understanding of the basic principles governing homogeneous electron transfer reactions. Starting with Marcus classical transfer theory and still going on today.
Usually these theories address ET from a localized single donor state D to a localized single acceptor state A.

$$D\,A \rightarrow D^{+}\,A^{-} \tag{2.1.1}$$

The electronic-nuclear coupling is strong and electron transfer is controlled by nuclear motion. The system moves on diabatic energy surfaces. Tunneling between reactant and product state occurs when both electronic levels are in resonance and the motion of the nuclei is the driving force to achieve this resonance.
In Marcus classical theory the nuclear motion is expressed in terms of harmonic oscillators for reactant and product state with identical frequency ν moving along a generalized reaction coordinate (RC) [4, 12]. RC accounts for the direction relevant for the ET process and is not necessarily identical to a bond in the molecule. The two diabatic energy surfaces for the reactant and product state are depicted in Fig. 2.1. The crossing point of the two parabola is called transition state (TS). In Fig. 2.1 (b) ΔG^{+} is the (unknown) activation energy, ΔG^{0} is the experimen-

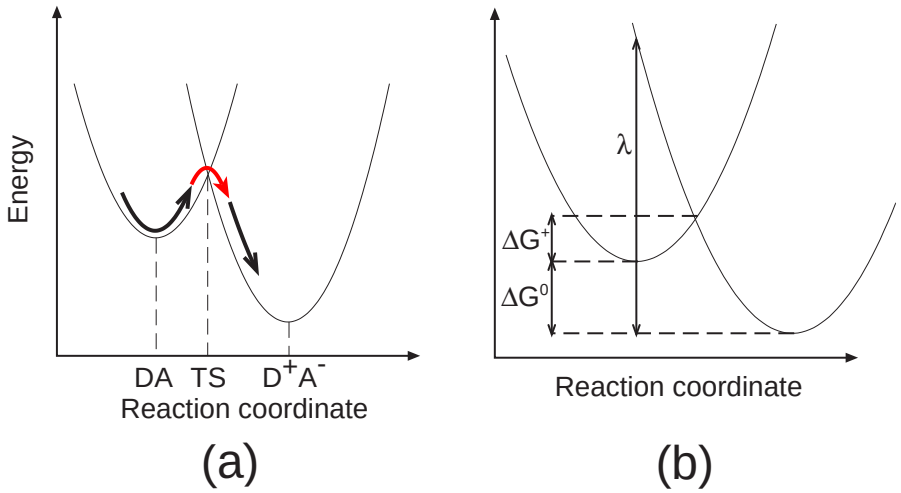

Figure 2.1: Diabatic energy surfaces for the reactant DA and product $D^{+}\,A^{-}$ state along the reaction coordinate RC.

tally available free energy of the reaction (Gibbs) of the transition and λ the reorganization energy. The latter is required to change the positions of all nuclei from the the equilibrated reactant state into the equilibrated product state while the electron resides on the donor. In case of a solvent environment the reorganization energy of the surrounding molecules has to be added to the intra-molecular reorganization energy and can exceed the latter for polar solvents.
In this picture the electron moves with the frequency of the harmonic oscillator back and forth in the reactant parabola, crossing the transition state twice per period. At the transition state there is a small (weak electronic coupling) probability for a transition to the product state. This is called the non-adiabatic limit. The quantum mechanical description is done in terms of first order perturbation theory. With a harmonic perturbation this leads to Fermi‘s golden rule:

$$k_{ET} = \frac{2\,\pi}{\hbar} V_R^2\; FC \tag{2.1.2}$$

V_R is the electronic coupling matrix element that is the weak perturbation of the system and FC is the Franck-Condon-weighted density of states. FC is the integrated overlap of reactant and product nuclear wavefunctions of equal energy. Going back to Marcus´ classical description FC can be expressed in terms of the probability of getting over the activation barrier with the thermal energy taken from the system. The activation energy is expressed in terms of the reorganization energy and the free energy of the reaction.

$$FC = \left(\frac{1}{4\,\pi\,\lambda\,k_B\,T}\right)^{\frac{1}{2}} \exp\left(-\frac{\left(\lambda + \Delta G^0\right)^2}{4\,\lambda\,k_B\,T}\right) \tag{2.1.3}$$

Inserting Eq. 2.1.3 into Eq. 2.1.2 results in the famous Marcus curve when plotting the rate against ΔG^0. This curve has a maximum when the free energy of the reaction is equal to the reorganization energy with the classically non-intuitive result that the reaction rate slows down when the free energy difference becomes larger. This has been verified experimentally for various systems [13, 14]. The effect is more easily understood from a quantum mechanical model involving Franck-Condon factors, as described below.
The classical description hold true as long as the effective frequency, determined by the slope of the parabolas, is slow and the thermal energy is high. Once $h\,\nu$ is equal or greater than $k_B\,T$ quantum mechanical corrections for FC are necessary. A semi-classical approach has been reported by Hopfield [15] resulting in a correction term for λ. A quantum mechanical extension for the intra molecular vibration has been given by Bixon and Jortner [16]. A first consequence

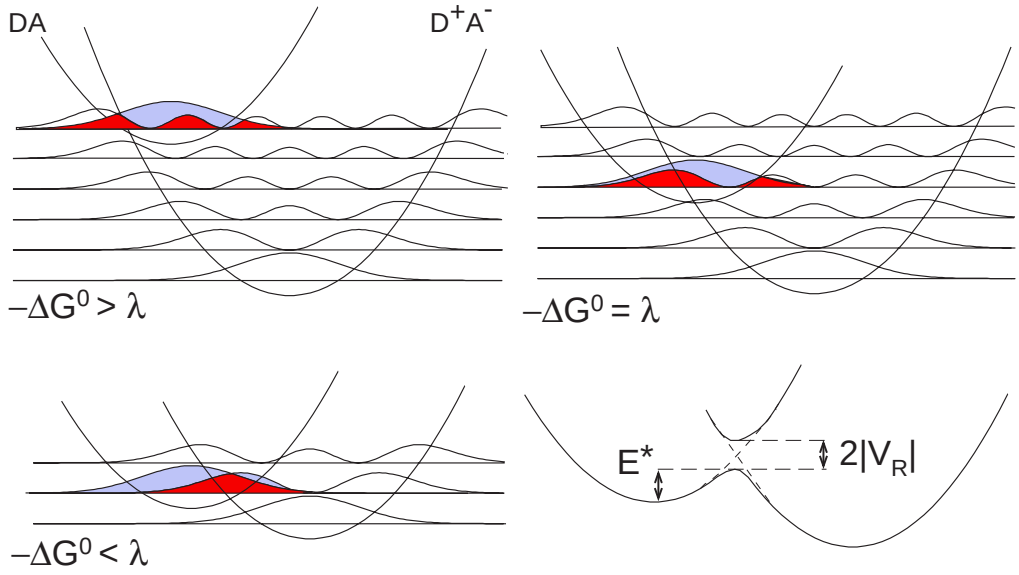

Figure 2.2: Harmonic oscillator nuclear wavefunctions squared for three different reaction-free energies. The Franck-Condon factors are proportional to the overlap (red area) of the reactant nuclear wavefunction squared with the product nuclear wavefunction squared which is maximal for $\lambda = \Delta G^0$. In the QM description the crossing of the two parabolas splits due to the avoided crossing of the electronic states.

from a quantum mechanically model is that the crossing point splits by $2\,|V_R|$ (Fig. 2.2 bottom right) where $|V_R|$ The Franck-Condon factors are proportional to the overlap (red area in Fig. 2.2) of the reactant nuclear wavefunction squared (blue area in Fig. 2.2) with the product nuclear wavefunction squared. In the high temperature limit the nuclear wavefunctions are localized at the classical turning points. Maximum overlap is achieved when the ground state of the reactant overlaps with the vibrational excited state of the product at the turning point. In Fig. 2.2 only the reactant ground state is shown, $h\,\nu > k_B\,T$. Since the overlap is still maximal for $\lambda = \Delta G^0$ it is obvious that the FC is not a continuous function of ΔG^0 for small temperatures.

The splitting of the adiabatic energies $2\,|V_R|$, and thus the electronic coupling, can be approximated by the splitting of the appropriate energy levels in a symmetrized system (Koopmans´ theorem [17]). Review articles on this subject can be found in Ref. [18, 19] also discussing the distance dependence of donor-bridge-acceptor systems and the nature of transport through bridges.

For the case where the bridge in a donor-bridge-acceptor systems has no electronic levels in the vicinity of the relevant transition state, a simple exponential dependence between ET rate and distance is expected following the exponential

decay of the electronic wavefunctions in the forbidden region occupied by the bridge:

$$V_R^2 = V_0^2 \exp(-\beta R) \ , \tag{2.1.4}$$

where R is the length of the bridge, β an exponential coefficient for the decay of the wavefunction and V_0 the maximum electronic coupling. This exponential relation has been verified for various systems experimentally ([20, 21] and references therein).

The above models holds true only when the electronic coupling is weak. That is, the probability of crossing the transition state is much smaller than 1 and thus, the frequency of the nuclear motion is much higher than the transfer rate. For strong electronic coupling, the so called adiabatic limit, the tunneling probability is nearly one and the electron follows the nuclear motion along the reaction coordinate. In this case one can no longer distinguish between reactant and product state (parabola), the splitting at the transition point gets bigger and the electronic wavefunction moves along the double-well potential composed of reactant and product potential. In presence of a solvent contributing a major part to the reorganization energy the ET rate is controlled by the solvent relaxation time T_S. The ET rate constant in the adiabatic limit can be expressed in terms of the effective barrier height E^* and the solvent relaxation time:

$$k_{ET} \propto \frac{1}{T_S} \exp\left(-\frac{E^*}{k_B T}\right) \tag{2.1.5}$$

The major difference between intramolecular homogeneous ET and heterogeneous ET from a molecular donor to a solid state acceptor is the number and energy of accessible acceptor states. Referring to Fig. 2.1 in the non-adiabatic limit, instead of one product parabola the reactant can couple to a whole series of product states with different ground state energies. Each product parabola represents the transferred electron in any electronic state as well as the ionized adsorbate molecule in the pertinent vibrational state. Of course, only those parabolas with a ground state energy lower than the reactant state contribute efficiently to the ET process. The transfer rate is proportional to the density of states below the reactant state. A special situation arises when the reorganization energy λ is equal or less than the energy difference between the reactant state and the bottom of the conduction band [1]. In this case every point of the reactant parabola is a transition state. Referring to Fig. 2.2 for every vibrational reactant state the overlap with any product state is maximal and the Franck-Condon factors sum

[1] Or the Fermi level in case of a metal.

up to 1. This situation is called "wide-band limit". Thus, in the wide-band limit the FC in Eq. 2.1.2 is formally replaced by a pure density of electronic states.

$$k_{ET} = 8\,\pi\,\hbar\,V_0^2\;DOS \tag{2.1.6}$$

Eq. 2.1.6 has been reported by Lanzafame et al. for a single reactant level coupled to a continuum of electronic product states with density of states DOS [22] and constant electronic coupling V_0 to all product states. k_{ET} in Eq. 2.1.6 reflects the strength of the electronic coupling. In the wide band limit Eq. 2.1.4 can be used to directly determine the decay parameter and the maximum coupling by varying the distance between the reactant and the product in the experiment.
The exact treatment of the time dependent injection process has been given by Ramakrishna et al. as the solution to the time dependent Schrödinger equation with a Hamiltonian describing the complete set of electronic-vibronic product states [23, 24]. The solution is the time and energy dependent density of electrons injected in the conduction band. The latter distribution has been measured for the first time making use of the unique properties of TiO_2. In a real solid the density of electronic states is a function of the energy and an integration has to be performed over an appropriate energy range whose width is determined by all the Franck-Condon factors, typically 0.5 eV to 1 eV wide.
In the non-adiabatic, wide-band limit of heterogeneous ET $\Delta\,G^+$ is always fulfilled for a particular product state. In this case a strong electronic coupling, i.e. a splitting of the levels at the crossing points, results in a barrierless double-well potential and an assignment of the electronic wavefunction to the donor or the acceptor side is not obvious and depends on the details of the time dependent experiment. Depending on the effective barrier height E^* substrate and molecular electronic levels will mix. When E^* becomes negligible one can no longer speak of ET but rather of dephasing between the adsorbate resonance and the continuum of substrate states.

2.2 Hot electron dynamics in metals and semiconductors

The dynamics of ET, discussed in the previous chapter, control the time scale for an excited electron to leave the molecule in heterogeneous systems. This is e.g. the decay of the molecular excited state measured in transient absorption measurements. 2PPE is in general not selective to either molecular or substrate

states and part of the 2PPE signal may originate from electrons already injected into the substrate. Therefore, the dynamics of excited electrons in solids are briefly discussed in this chapter. The first part of this section deals with hot electron dynamics in general with a focus on metals. In the second part some peculiarities of hot electron dynamics in semiconductors are discussed. Detailed treatments are found e.g. in Refs. [1, 25, 26].

A short laser pulse impinging on the bare surface of a single crystal will generate a coherent distribution of excited electrons and the corresponding distribution of holes below the Fermi level. This distribution will resemble the superposition of the spectrum of the laser pulse and the joint density of states (JDOS) of occupied and unoccupied states. At first, the collective response of the excited carriers builds up resulting in Coulomb screening of the bare charges. This process takes place on a time scale comparable to the inverse plasma frequency [27]. Right after excitation scattering of the coherently excited electron-hole pairs will destroy the coherence and generate a non-thermal population of excited electrons and holes. Electron-electron scattering will redistribute the momenta of this electron ensemble to form a Fermi-Dirac distribution with a certain temperature which may be much higher than the temperature of the lattice. The time scale for e-e scattering in a free electron gas can be estimated from the lifetime of a single excited electron. From Landau´s Fermi liquid theory it follows that the lifetime is proportional to $(E-E_{Fermi})^{-2}$ [28]. This is in good agreement with the energy dependence of the inelastic lifetime measured e.g. in Ag but fails to describe the energy dependence of the inelastic lifetime measured in transition metals [29]. Due to the difference in heat capacity between the electron system and the lattice it is possible to create an extremely hot electron distribution by excitation with an ultra short laser pulse [2]. The hot electron distribution will cool down by loosing energy via electron-phonon (e-p) scattering until it reaches equilibrium with the lattice. However, the time scales for e-e and e-p scattering are not necessarily well separated. Experimental investigations have shown, that in general the thermalization of the distribution via e-e scattering is not completed before cooling via e-p scattering sets in [30]. Fann et al. [31, 32] have shown, that hot electron relaxation in gold can not be described properly with the diffusive two-temperature model [33] and used a Boltzmann transport model which explicitly includes the nonthermal part of the distribution to fit the experimental data. A review of the Boltzmann formalism for excited electron dynamics in metals is

[2]The photon density for a 150 kHz lasersystem is about $1 * 10^5$ higher than for a cw laser with the same output power. While in the first case the density of excited electrons is of the order of $1*10^{18}$ cm^{-3} the electron density drops by a factor of $1 * 10^5$ for cw excitation. At such densities thermalization by electron-electron scattering is no longer possible

given in Ref. [34]. The time scales for the different processes in metals discussed above are depicted in Fig. 2.3.

In principle, all the above mentioned processes can be observed in TR-2PPE

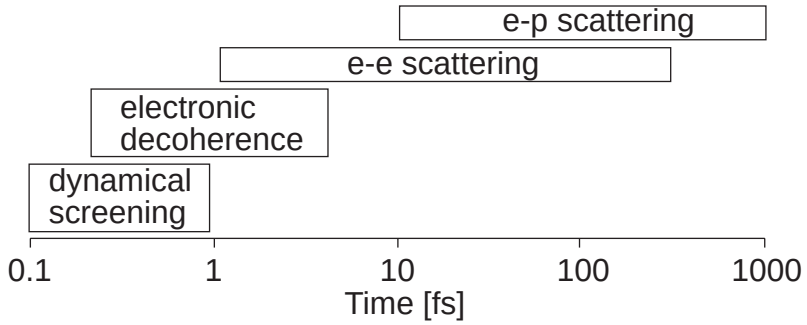

Figure 2.3: The time scales for various different processes in metals. Taken from Ref. [1].

experiments. However, the time dependent signal at a certain kinetic energy does not resemble the lifetime of the pertinent excited electrons exactly. Two major mechanisms have to be taken into account to interpret the TR-2PPE signal correctly:

The population in a particular level above the conduction band is not only described by the scattering of electrons out of the level. Refilling of the level happens via two processes: scattering of electrons from higher energies and generation of secondary electrons by an Auger process. These processes are depicted in Fig. 2.4. Both processes are slowing down the decay of the 2PPE signal. The latter has attracted much attention in connection with TR-2PPE measurements on Cu where an unusual peak in the relaxation time was observed and ascribed to Auger electrons created by the refilling of d-band holes [34, 35, 36].

The second mechanism that has to be taken into account in TR-2PPE measurements is the escape of electrons from the detection range. The detection range in photoemission spectroscopy is determined by the escape depth of electrons rather than by the penetration depth of the light as the former is much shorter in general. For transport out of the detection range only the propagation perpendicular to the surface $v_\perp$ is of relevance since the size of the laser spot ($\sim 100\ \mu m$) is orders of magnitude larger than the escape depth ($\sim$ 30 Å). For the non-thermal part of the electron distribution (early times) the transport is ballistic. The velocity $v_\perp$ can be estimated by the Fermi velocity (v_F=15 Ås^{-1} in Cu) and the excitation profile by the penetration depth of the pump pulse (d_p=15 nm, hν=3 eV in Cu) to get a rough estimate for the time scale of ballistic transport: $\tau_{bal} = d_p/v_F$ =10 fs. Thus, for lifetimes of some 10 fs the transport effect has to

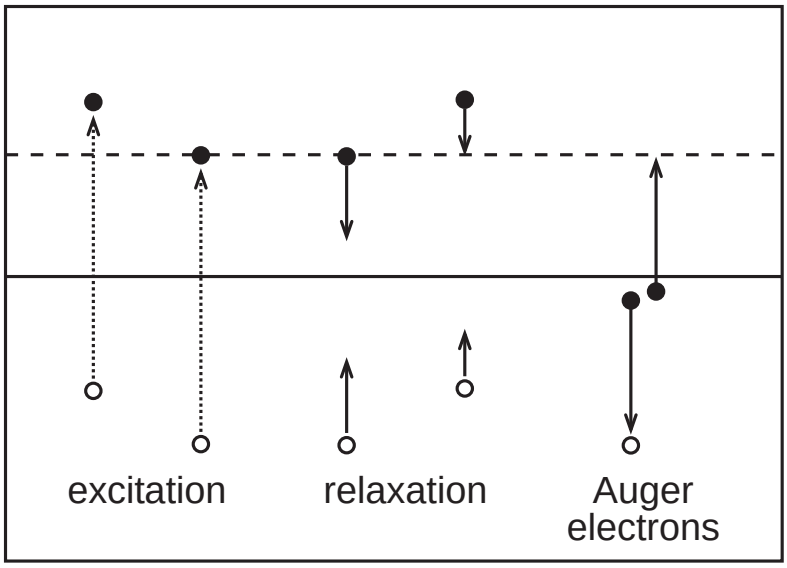

Figure 2.4: Generation of secondary electrons.

be taken into account. The thermal part of the electron distribution (later times) can be described by diffusive motion:

$$\dot{N}_e = D_e \frac{\mathrm{d}^2 N_e}{\mathrm{d}z^2} + S\,(z,t) \tag{2.2.1}$$

Where N_e denotes the electron density, D_e the diffusion coefficient and S the generating term, i.e. the pump pulse. D_e can be obtained via the Einstein relation $\mu\, k_b\, T/e = D_e$ from the mobility (μ=22 $cm^2V^{-1}s^{-1}$ for Cu). If the diffusion length is identified with the penetration depth the characteristic time scale for a 1000 K hot electron distribution is $\tau_{dif} = d_p^2/D_e \sim 1$ ps. Thus, diffusive transport becomes important at much later times than ballistic transport. Various measurements and theoretical models with different levels of sophistication concerning the "transport effect" have been reported [37, 38, 35, 29, 34, 39] and have shown that this effect is not negligible.

When the solid is a semiconductor the presence of the bandgap and the different degree of screening have a strong influence on the relaxation times. The former is due to the reduced phase space for scattering with electrons in the Fermi sea. The latter due to the enhanced scattering cross section. A review of carrier transport is given in e.g. [40].

A detailed investigation of hot electron dynamics in InP has been carried out in our group in collaboration with the theory group of Prof. Knorr [41, 42]. The thermalization time for InP was found to be less then 300 fs at a carrier density of 10^{-18} cm^{-3}.

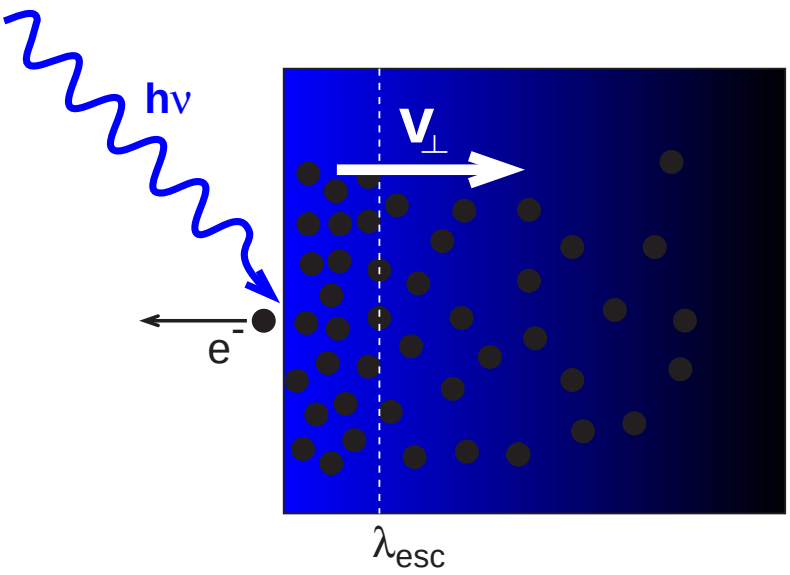

Figure 2.5: Escape of electrons from the detection range given by λ_{esc}.

However, it will be shown in this work that the dynamics of excited electrons in TiO_2 differ significantly from those measured in III-V semiconductors. A detailed discussion of electron dynamics measured on the bare TiO_2 surface is given in Sec. 4.2.2.

2.3 Energy level alignment at adsorbate substrate interfaces

For determining the relative positions adsorbate electronic levels and substrate bands, vacuum level (VL) and ionization potential (IP) are important values. Although the simple approach of matching the ionization potential of the molecule at the work function of the substrate mostly fails, the vacuum level is worth looking at more closely [43, 44, 45].
The vacuum level is simply the energy of an electron at rest positioned at infinite distance from the system and the work function is defined as the energy difference between the Fermi level and VL. But right at the surface, the potential is affected by the microscopic distribution of charges. For example the work function is different on different surfaces of a metal single crystal, e.g. silver has work functions of 4.45 eV, 4.5 eV, and 4.8 eV for the (100),(110), and (111) surface. Since the Fermi level is a bulk property, these differences reflect the different VLs at the different surfaces. For metals, these differences are explained by the different

amount the electron cloud laps out of the surface, leading to a dipole layer at the surface. Of course the latter will be affected by an adsorbate layer, e.g. the lowering in work function of metal surfaces covered with rare gases is attributed to the electron cloud being pushed back by the rare gas atoms.
The nature of level alignment at interfaces strongly depends upon the materials in contact. At metal/metal interfaces one would call it an ohmic contact. The Fermi levels will align because of a sufficient density of free electrons and the VLs - and all the other bands - will bend at the interface. For thin organic layers, i.e. several monolayers, on metal or semiconductor surfaces the number of mobile charge carriers is restricted and since the HOMO-LUMO gap of the layer is much larger than the thermal energy in most cases no charge redistribution will occur and flat band situation is expected.
For separated substrate:organic-layer systems the levels will match at the VL at

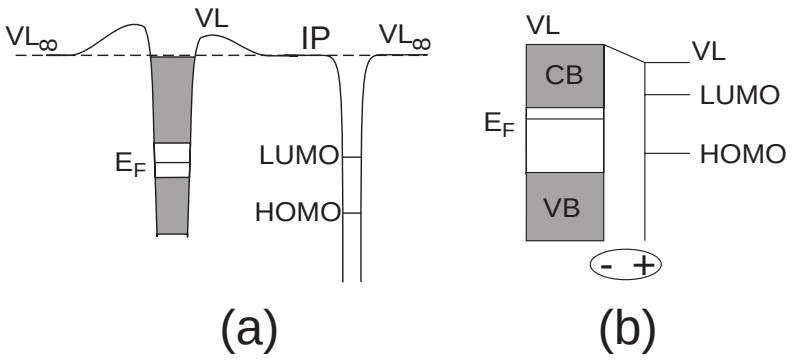

Figure 2.6: (a) Level alignment between a semiconductor (left) and a molecule at VL_∞ at infinite distance. The vacuum near the semiconductor is changed due to surface effects. (b) Level alignment of a molecule on the surface of a semiconductor. The surface dipole shifts the VL.

infinity (Fig. 2.6 (a)). Bringing both systems together without rearrangement of the charges, the alignment will take place at the VL right at the interface, resulting in a shift of HOMO and LUMO level with respect to the Fermi level. But in general there will be a redistribution of charges due to various mechanisms like: charge transfer, mirror forces, surface rearrangement and chemical interaction. The redistribution of charges leads to a dipole layer at the interface and to a shift of the VL.
The organic layers investigated in this work were all at a sub-monolayer to monolayer coverage. Thus, band bending can be excluded in all systems. All molecules were chemically anchored on the substrate. Therefore, a dipole layer due to the formation of the chemical bonds is expected. The resulting alignment scheme is

depicted in Fig. 2.6 (b). Level alignment for the different systems under investigation is discussed in detail in Sec. 4.1.

2.4 Time-resolved two-photon photoemission spectroscopy

Time-resolved two photon photoemission is a unique tool for studying the electronic structure and dynamical processes at interfaces. Review articles are found in Refs. [26, 1, 46]. In principle two photons interact with an electron where the second interaction lifts the electron above the vacuum level of the sample. Under certain conditions this electron can leave the sample and is detected with an analyzer. The second step is essentially the same as in single photon photoemission and the numerous text books on photoelectron spectroscopy provide an appropriate basis for the understanding of the two-photon photoemission process [47, 48].

Time resolution is achieved by delaying one pulse against the other. The 2PPE signal will then reflect the population dynamics of the intermediate state in the delay-dependent electron yield. Such measurements are referred to as "pump-probe" measurements where the pump pulse populates an intermediate state and a delayed probe pulse probes the population. The 2PPE process is illustrated in Figure 2.7. As an example the level scheme of the Cu(111) surface with an occupied surface state n=0 and an unoccupied surface state n=1 located in the surface projected band gap is depicted. In principle three different kind of states can be probed with 2PPE: initial states if the intermediate state has virtually no lifetime and is thus energetically not localized, intermediate states with a finite lifetime that are in some way populate with the first pulse, and final states localized above the vacuum level of the sample and auto-ionizing with a certain probability. In monochromatic 2PPE, i.e. both photons have the same energy, these different contributions can be distinguished by varying the photon energy. The initial state will shift with twice the photon energy, the intermediate state with just the the photon energy, and the final state will not shift at all. For bichromatic 2PPE this procedure is possible too, but both wavelengths have to be varied. However, only the intermediate states can yield a delay dependent signal not resembling the cross-correlation of both pulses. Moreover, the assignment of the photon energies to pump and probe pulse is evident once a deviation of the temporal evolution of the 2PPE signal from the CC is observed. It should be noted that in general there is an upper limit to the photon energy in 2PPE

experiments, once it exceeds the work function E_Φ=E_{Vac}-E_F one-photon emission will cover the 2PPE emission.

An advantageous property of photoemission in general is the conservation of

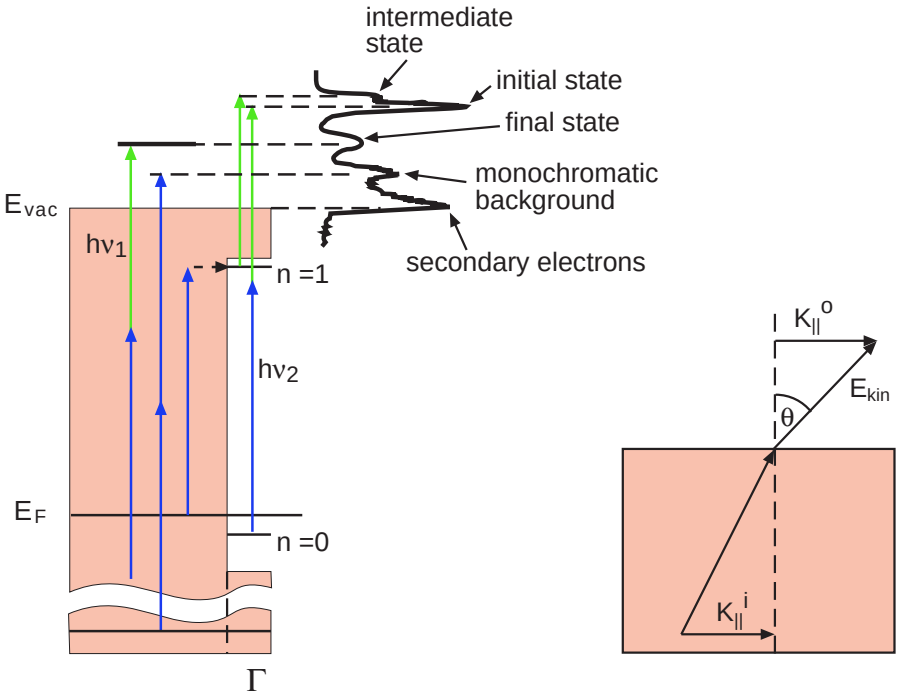

Figure 2.7: Left: Possible 2PPE processes (the final state was added to the picture). Right: Conservation of the parallel momentum in the photoemission process.

the momentum parallel to the surface, whereas the perpendicular momentum changes because of the potential step at the surface. Thus, angle-resolved 2PPE is capable of measuring the dispersion of states parallel to the surface plane, e.g. bulk and adsorbate bands, and image potential states. The relationship between the parallel momentum of an electron and its kinetic energy E_{kin} when emitted under an angle θ reads:

$$k_\parallel = \left(\frac{2m_e\, E_{kin}}{\hbar^2}\right)^{\frac{1}{2}} \sin\theta \tag{2.4.1}$$

Where m_e is the electron mass and the momentum of the photon is neglected. The dispersion of a state can be often expressed in terms of the effective mass m_{eff}.

$$\frac{1}{\mathbf{m}_{eff}} = \frac{1}{\hbar^2}\frac{\partial^2 \mathbf{E}}{\partial \mathbf{k}^2} \tag{2.4.2}$$

In the vicinity of $k_\parallel = 0$ and small $k_\parallel$ the dispersion can be approximated with a parabola and m_{eff} is a scalar.

$$E(k_\parallel) = E(k_\parallel = 0) + \frac{m_{eff}}{m_e} k_\parallel^2 \tag{2.4.3}$$

2.4.1 Rate equations and optical Bloch equations

To model the measured TR-2PPE spectra two approaches are common. One possibility is fitting the signal with simple kinetic models, i.e. rate equations, the other is modeling via optical Bloch equations. The latter has the advantage of including coherence effects. A three level optical Bloch scheme, containing the initial, intermediate and final state, has been used by Knoesel et al. to model TR-2PPE from surface states [49]. Here we will use an even simpler model. TR-2PPE will be treated as a two-step process. For the first step, i.e. populating the intermediate state, a two level Bloch model is used, connecting initial and intermediate state. The second step, i.e. probing the intermediate state population, is incorporated as the convolution of the intermediate state population with the probe pulse. Such a scheme has successfully been used to model coherence effects in the pump step [50]. Moreover, separating the 2PPE process and neglecting coherence effects once the polarization has decayed has been justified by elaborate second-order response theory by Timm et al. [51].
A description of light-matter interaction is usually given in terms of a density matrix approach [52]. The discussion will be restricted to a two level system. Initial $|0\rangle$ and intermediate $|1\rangle$ state are the only states of the unperturbed Hamiltonian H_0 interacting with the field of the pump pulse $V(t)$. The Liouville-von-Neumann equation describing the temporal evolution of the density matrix reads:

$$i\hbar \frac{\mathrm{d}\rho}{\mathrm{d}t} = [H_0 + V, \rho] - \Gamma\rho \tag{2.4.4}$$

Where Γ is the dissipation of the system and $V(t)$ the perturbation due to the classical light field $\vec{E}$ interacting with the dipole moment $\vec{\mu}$:

$$V(t) = \vec{\mu} \cdot \vec{E} \tag{2.4.5}$$

From Eq. 2.4.4 in the dipole and rotating wave approximation four coupled ODEs are obtained:

$$\begin{aligned}
\dot{\rho}_{11} &= -\gamma_1\,\rho_{11} + A\,\rho_{22} - i\,\frac{\chi}{2}\,(\rho_{12} - \rho_{21}) \\
\dot{\rho}_{12} &= -\left(\beta - i\,\delta\right)\,\rho_{12} + A\,\rho_{22} + i\,\frac{\chi}{2}\,(\rho_{22} - \rho_{11}) \\
\dot{\rho}_{21} &= \dot{\rho}_{12}^{*} \\
\dot{\rho}_{22} &= -\left(\gamma_2 + A\right)\,\rho_{22} + i\,\frac{\chi}{2}\,(\rho_{12} - \rho_{21})
\end{aligned} \tag{2.4.6}$$

Where $\chi = \vec{\mu} \cdot \vec{E}/\hbar$ is the Rabi frequency, γ_i are the inelastic scattering rates, δ is the detuning between transition energy and photon energy, A the rate of spontaneous emission and $\beta = \gamma_E + \frac{1}{2}\,(\gamma_1 + \gamma_2 + A)$, with γ_E the rate of elastic collisions. The diagonal elements account for the populations of the respective states and are real numbers, while the imaginary off-diagonal elements contain the phase information. The solutions of Eq. 2.4.6 can show various behaviors depending on the choice of the parameter. For our application some restrictions can be made:

- for the short laser pulses used in the experiment $\vec{E}$ is substituted by the envelope of the electric field of the pump pulse $\vec{E}(t)$
- the field strength in the experiment is sufficiently low such that Rabi oscillations can be neglected, that is $\int_{-\infty}^{\infty} \chi(t) \ll \pi$.
- from this it follows that the population of ρ_{11} can be treated as constant: $\rho_{11} = 1$, $\dot{\rho}_{11} = 0$
- there is no inelastic scattering in the ground state and the time scale of the experiment is short such that spontaneous emission can be neglected

With these restrictions Eq. 2.4.6 reads:

$$\begin{aligned}
\dot{\rho}_{22} &= -\frac{1}{T_1}\rho_{22} - i\frac{\chi(t)}{2}\,(\rho_{12} - \rho_{21}) \\
\dot{\rho}_{12} &= \left(i\delta - \frac{1}{T_2}\right)\rho_{12} - i\frac{\chi(t)}{2}\,(\rho_{22} - 1)
\end{aligned} \tag{2.4.7}$$

T_1 is the relaxation time of the system and $T_2 = (1/T_2^{*} + 1/2\,T_1)^{-1}$, where T_2^{*} is the pure dephasing time. For $T_2^{*} \to 0$ Eq. 2.4.7 becomes a rate equation. The main difference between the solutions of Eq. 2.4.7 for finite dephasing times and a rate equation is a delayed rise of the population in ρ_{22}. This difference is the

main reason for using the Bloch model to account for the initial step in TR-2PPE. Once the exact position of time zero (t_0), i.e. the delay for which the centers of both pulses overlap, is exactly known, it is possible to extract both time constants from a fit with the Bloch model. However, determination of the exact t_0 is not always possible, because the cross-correlation can not be measured exactly at the sample position. Even some 10 cm of air can change the delay between two pulses by some fs depending on the differences in their wavelengths.
TR-2PPE measurements have the advantage that the determination of t_0 is often possible on the sample itself. The TR-2PPE signal resembles the cross-correlation of the pulses at a particular kinetic energy for many samples. In this case, the relaxation time, and simultaneously the dephasing time, of the particular intermediate state are much shorter than the pulse duration. In that way it is possible to extract the exact position of t_0. Provided that the time resolution is sufficiently good, it is possible to extract both time constants, i.e. relaxation and dephasing time, from a fit with the Bloch model. However, for most of the systems discussed here it was not possible to extract a dephasing time because the latter was too short to be resolved.
As mentioned above, the probe step was incorporated by convolution of the intermediate state population with the intensity of the probe pulse. Thus, the TR-2PPE yield reads:

$$\omega_{2PPE}(t_d) \propto \int_{-\infty}^{\infty} \rho_{22}(t)\, I_{probe}(t - t_d)\, \mathrm{d}\, t \tag{2.4.8}$$

2.5 Ultrafast spectroscopy

Ultrafast laser spectroscopy is one of the most recently developed experimental technique in physics and represents by itself a field of active research. For a review of this extensive field see e.g. Ref. [53]. This section focuses on the following two experimental setups that were build in our lab as part of this work:

- The *Noncollinear Optical Parametric Amplifier* (NOPA) for generation of ultrashort laser pulses

- The *Spectral Phase Interferometer for Direct Electric field Reconstruction* (SPIDER) used to characterize ultrashort pulses in time and phase

2.5.1 Generation and characterization of ultrashort laser pulses

The laser pulses used in this work were ten to fifty femtoseconds (fs) long. The duration Δt of a laser pulse is limited by its spectral width $\Delta\nu$ due to the Fourier transformation. The time-bandwidth product reads

$$\Delta\nu\Delta t \geq C \tag{2.5.1}$$

where C is a factor that depends on the shape of the pulse [3]. Identity in Eq. 2.5.1 is obtained when the phase is constant across the pulse. It is obvious that one needs broad spectra to generate short pulses and that the different spectral components must overlap in time. Unfortunately, this temporal overlap is destroyed by dispersive elements like lenses, windows and filters and even the dispersion of air comes into play when dealing with pulses as short as 15 fs. Dispersion leads to a lengthening of the pulse and to a characteristic sequence of the spectral components called *chirp* where the red components are traveling faster in normal dispersive elements and arrive first and the blue components arrive last.

Noncollinear Optical Parametric Amplifier Optical parametric amplification is a nonlinear optical effect where a pump and a signal photon interact in a nonlinear crystal and generate two signal and one idler photon. By means of energy conservation this is written as:

$$\omega_s + \omega_p = 2\omega_s + \omega_i \tag{2.5.2}$$

In addition momentum conservation requires

$$\Delta k = k_p - k_s - k_i = 0. \tag{2.5.3}$$

This is the so called *phase matching condition* and is fulfilled by adjusting the optical axis of a nonlinear crystal. Unfortunately, phase matching does not ensure matching of the group velocities and the different frequencies disperse inside the crystal. Due to the Fourier limit, generation of ultrashort pulses requires broadband amplification of the signal pulse. This is achieved once the change of

[3] e.g. a Gaussian pulse has C=.4413

Δk with the signal wavelength is zero [54].

$$\frac{\partial \Delta k}{\partial \lambda_s} = 0 \tag{2.5.4}$$

This can be expressed in terms of the angle between signal and idler wave inside the crystal and the group velocity:

$$v_{g,i} \cos \Omega = v_{g,s}. \tag{2.5.5}$$

The above requirement is achieved by overlapping the signal and pump pulses

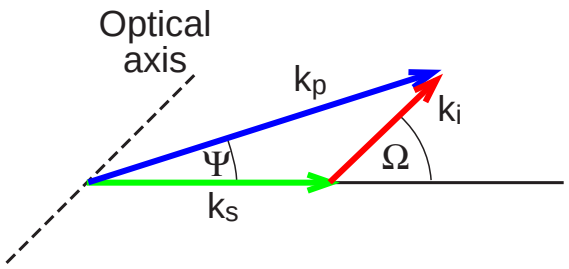

Figure 2.8: Crystal internal angles and momenta.

with a certain tilt angle Ψ in the crystal.
The design and performance of the two NOPA setups used for this work is described in detail in Sec. 3.1.

Auto- and crosscorrelation Femtosecond laser pulses are too short to be characterized in time directly (e.g. with a diode). The most common way to measure the temporal width of a pulse is taking the autocorrelation trace in a χ^2 process. This is often done by generating the second harmonic generation (SHG) signal between two variable time delayed pulse replicas. For spectrally broad pulses, this has to be done with care. Due to the limited spectral acceptance of non-linear crystals like BBO only part of the spectra is frequency mixed and the autocorrelation becomes too narrow in time [55].
Recently, silicon carbid photodiodes have become available, which offer a large bandgap, such that in the visible range a two photon process is necessary to generate a photocurrent. This process is also a χ^2 process, but it is not spectrally selective and thus more trustworthy.
For UV pulses, these diodes are not applicable because the bandgap is too narrow. Therefore, autocorrelation traces were measured with TR-2PPE on the bare surface of a copper (111) single crystal via resonant photoemission from the oc-

cupied surface state. This method is described in detail in Sec. 4.2.1.
The crosscorrelation between two pulses with different photon energies was measured in the same way. Both, the two-photon excitation in SiC and the two-photon photoemission in TR-2PPE depend only on the sum of the two photon energies and no phasematching conditions are necessary.

Spectral Phase Interferometer for Direct Electric field Reconstruction (SPIDER) Especially when dealing with spectrally broad pulses the knowledge of the temporal [4] phase becomes important for compressing such pulses to sub 15 fs. A widespread method is *Frequency Resolved Optical Gating*, where the autocorrelation trace is also resolved spectrally. The disadvantage of the latter method is that the FROG trace is not unique and sometimes hard to interpret. Moreover, FROG requires an iterative procedure to reconstruct the electric field. The SPIDER method yields instead the complete information about the electric field. It was presented by C. Iaconis and I. A. Walmsley in 1998 [56]. SPIDER is an interferometric method not requiring a known reference field. The reconstruction of the field is non-iterative and therefore fast. The setup has a collinear geometry and no moving parts are necessary. The spider apparatus is shown in Fig. 2.9. At the face of a parallel plate of a dispersive medium the

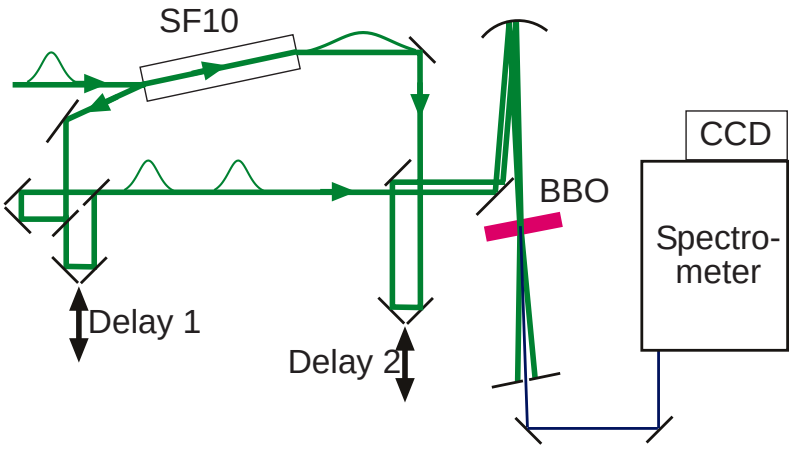

Figure 2.9: The spider apparatus. For details see text.

pulse is split in two parts. The major part passes through the glass block and is severely chirped. The rest of the pulse is reflected and split into two equal replicas in a Michelson interferometer. These two pulses can be delayed with respect to each other via delay 1. The second delay 2 is used to overlap in time

[4] or spectral, since it is the Fourier transformed

the two replica with the sheared pulse to generate two upconverted pulses in a BBO crystal. Due to the spectral chirp of the stretched pulse the two replicas are mixed with slightly different frequencies and consequently the upconverted pulses are spectrally sheared to one another. The upconverted pulses interfere inside a monochromator. The interference pattern is recorded and analyzed in order to obtain the spectral phase.
The electric field of the first pulse reads:

$$E_1(\omega) = |E(\omega)|\, e^{i\Phi(\omega)}. \tag{2.5.6}$$

The electric field of the second pulse reads:

$$E_2(\omega) = |E(\omega-\Omega)|\, e^{\imath(\Phi(\omega-\Omega)+\tau\omega)}. \tag{2.5.7}$$

With τ being the delay with respect to the first pulse and Ω the spectral shear of the stretched pulse. The interferogram measured inside the spectrometer is given by:

$$D_{\Omega,\tau} = |E_1(\omega) + E_2(\omega)|^2\,. \tag{2.5.8}$$

Substitution of the electric fields and simplification yields:

$$\begin{aligned} D_{\Omega,\tau} &= |E(\omega)|^2 + |E(\omega-\Omega)|^2 + 2\,|E(\omega-\Omega)E(\omega)|^2 \\ &\quad \cdot\cos\big(\Phi(\omega-\Omega) - \Phi(\omega) + \tau\omega\big) \end{aligned} \tag{2.5.9}$$

The argument of the cosine $\big(\Phi(\omega-\Omega)-\Phi(\omega)+\tau\omega\big)$ contains the information about the spectral phase. It is the deviation $\Phi(\omega-\Omega)-\Phi(\omega)$ from a constant distance $\tau\omega$ between the fringes of the interference pattern. The *phase difference* θ is obtained by Fourier transformation of the spectrum. A Fourier back-transformation of the temporal sideband results in a fringe pattern without the Gaussians envelope. Subtraction of a calibration with $\Omega = 0$ results in the spectral phase difference [5]. If the shear Ω is small compared to the structure of the spectral phase Φ, one can approximate:

$$\begin{aligned} \theta(\omega) &\equiv \Phi(\omega) - \Phi(\omega-\Omega) \approx \Omega\frac{\mathrm{d}\Phi(\omega)}{\mathrm{d}\omega} \\ \Rightarrow\quad \Phi(\omega) &\approx \frac{1}{\Omega}\int \mathrm{d}\omega\theta(\omega) \end{aligned} \tag{2.5.10}$$

Knowledge of the spectral phase $\Phi(\omega)$ is particularly useful if the chirp is to be controlled via "deformable mirrors"[57]. These are electrostatically deformable

[5] A measurement with the stretched pulse blocked.

membranes coated with a reflecting layer. Deformable mirrors allow for adjusting the spectral phase by changing the path length of the individual frequency component when used as end mirrors in a prism compressor.
The setup described above was implemented by the author and turned out to give reliable results for the pulse length compared with AC measurements. A disadvantage of the SPIDER setup is the space consuming spectrometer and interferometer. Thus, the pulse characterization can hardly be done near the sample position. The necessary difference in the overall path length for the pulses significantly changes the chirp due to the dispersion in air. Another disadvantage is the time consuming adjustment procedure. Because of the two disadvantages auto- and crosscorrelation measurements (Sec. 2.5.1) were rather used for everyday pulse characterization. Whereas reliable pulse widths were obtained from measurements with the SiC diode or TR-2PPE on a Cu(111) sample, informations concerning the phase of the pulses were not at hand using latter methods.

2.6 Experimental systems

To investigate the electron transfer dynamics and subsequent processes in the near surface region of the substrate different combinations of molecules and substrates were used. Whereas most measurements have been done with perylene derivatives attached to the (110) surface of rutile TiO_2, additional investigations of a catechol:rutile and a perylene:Ag system were of fundamental importance to gain insight into the different processes observed with TR-2PPE.

2.6.1 The molecules

The main desired properties of the molecules for investigating heterogeneous electron transfer are the relative positions of ground and excited state with respect to the band structure of the substrate and, for practical implementation, the accessibility of the required wavelength with available light sources.

2.6.1.1 Perylene

Perylene is a polycyclic, planar hydrocarbon with point group $D2_h$. The structure is shown in Fig. 2.10. This molecule has been intensively investigated by our group by means of standard stationary methods as well as transient absorption spectroscopy. Attached to TiO_2 anatase colloids it serves as a model system for

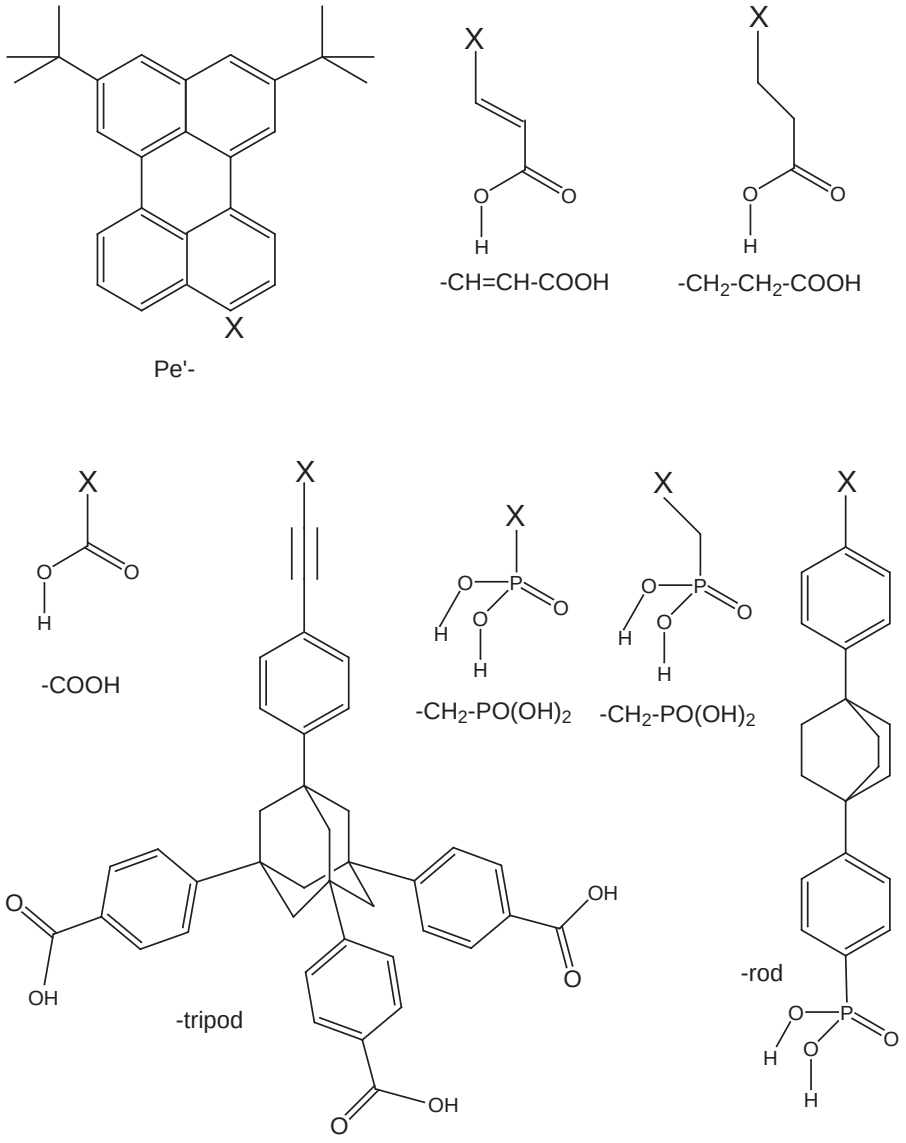

Figure 2.10: Structural formula of perylene and the different spacer and anchor groups.

the electron injection process in the so called Grätzel solar cell [5]. For the purpose of optical spectroscopic methods the well separated absorption spectra of ground state, exited state and cationic state in the visible range (Fig. 2.11) gave one of the main reasons for choosing this molecule. The absorption above 350 nm is assigned

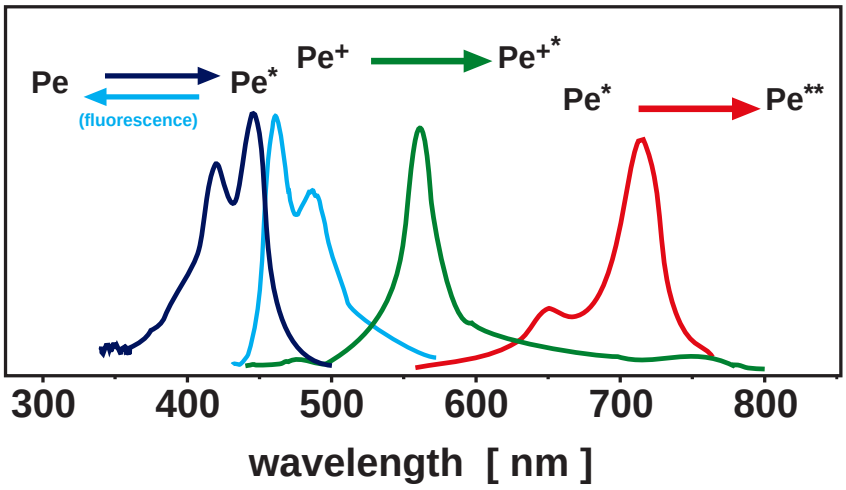

Figure 2.11: Absorption and emission spectra of perylene: ground state absorption (blue), S_1-S_0 emission (cyan), cation absorption (green), excited state absorption (red).[58, 59, 60, 61]

to the Franck-Condon broadened $S_0(^1A_g)$- $S_1(^1B_{3u})$ transition with symmetry B_{3u}. The neutral excitation is a single HOMO - LUMO transition with the transition dipole along the long molecular axis [62]. Another important property for measuring electron transfer dynamics is the absence of competing processes like inter- system crossing. For perylene, the quantum yield of fluorescence is above 90 % [63] and the fluorescence lifetime is nearly 5 ns and thus orders of magnitude longer than the time scale of the processes discussed in this work. Thus, heterogeneous electron transfer is the only relevant de-excitation process for the molecule on the surface up to the picosecond range.

The perylene chromophore was chemically modified:

- to prevent aggregation of the molecules in solution and on the surface, a tertiary butyl group was inserted in 2 and 5 position, respectively. These bulky groups make the interaction of the delocalised π orbitals of two neighboring molecules insignificant. This is verified by the diminished fluorescence quenching in solution. The perylene chromophore with substituted tertiary butyl groups will be abbreviated as Pe'.

- to anchor the molecule via chemisorption on the surface of TiO_2, an acid

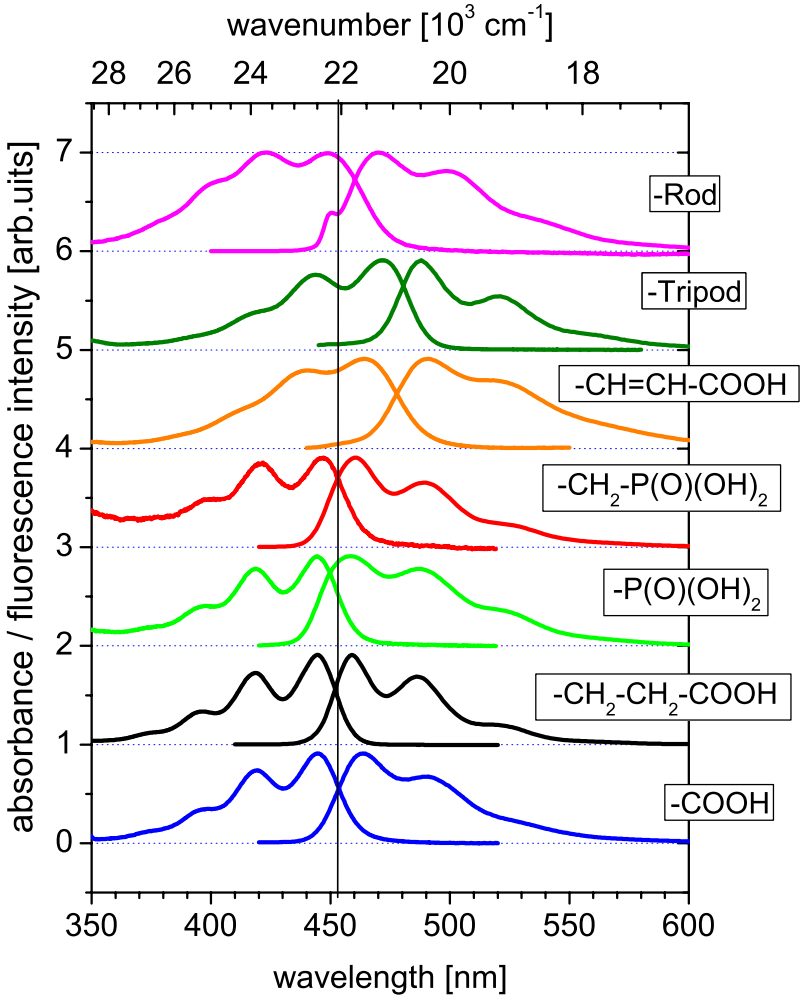

Figure 2.12: Normalized absorption and emission spectra of the perylene derivatives in a solution of toluene (50 %) and methanol (50 %). The concentrations for the absorption spectra were around 10^{-5} M. The emission spectra were taken with an excitation wavelength of 410 nm (dye-concentrations $\sim 10^{-6}$ M). Absorption and emission spectra of the different Pe' derivatives are taken in part from Ref. [64]

Compound name	S_0-S_1 transition energy [eV]
Pe'-COOH	2.74
Pe'-CH=CH-COOH	2.60
Pe'-CH_2-CH_2-COOH	2.75
Pe'-tripod	2.58
Pe'-CH_2-$PO(OH)_2$	2.74
Pe'-$PO(OH)_2$	2.76
Pe'-rod	2.70

Table 2.1: S_0-S_1 transition energies for the different perylene derivatives.

group is attached in 9 position.

- to investigate the effect of the distance between the chromophore and the semiconductor surface on the ET process, spacer groups were inserted between the chromophore and the anchor group.

- The effect of the acid group was investigated by exchanging carboxylic for phosphonic acid.

The perylene derivatives shown in Fig. 2.10 were synthesized by W. Storck (Fritz-Haber-Institut Berlin, HMI Berlin) and S. Felber (HMI Berlin). Details of the synthesis can be found in Ref. [65]. The tripod unit was provided by the group of E. Galoppini, Rutgers University, and attached to the perylene chromophore by S. Felber [66].
Stationary absorption and emission spectroscopy of the perylene compounds in solution together with semi-empirical RHF ZINDO/S calculations were performed to investigate the influence of the different substituents with respect to the S_0-S_1 transition [64]. As expected, the tertiary butyl groups turned out to be not involved in the optical transition. ZINDO/S calculations show that neither the HOMO nor the LUMO orbital are delocalized into the tertiary butyl group. The influence of the spacer/anchor group on the absorption and emission spectra depends on the chemical nature of the spacer group [64]. For saturated, sp^3-hybridized spacer groups and the directly linked anchor groups the effect is little since again the HOMO and LUMO orbital are not affected much by the spacer group. Consequently, only minor changes were observed in the absorption and emission spectra for Pe'-COOH, Pe'-CH_2-CH_2-COOH, Pe'-$PO(OH)_2$ and Pe'-CH_2-$PO(OH)_2$ (Fig. 2.12). The situation changes when the perylene molecule

is attached to an sp^2-hybridized spacer. The excited state orbital partly extents into the spacer group leading to a red shift in the absorption and emission spectra of Pe'-CH=CH-COOH, Pe'-tripod and Pe'-rod (Fig. 2.12).
Absorption spectra were also recorded for some of the molecules adsorbed on anatase colloidal films [64]. The spectrum of Pe'-COOH exhibited a pronounced change. The Franck-Condon progression is completely washed out. Wang et al. have reproduced this spectrum with a model that considers only the dominant vibrational mode [67]. The broadening was correlated with the fast injection time of 13 fs. Similar results have been reported for Pe'-CH=CH-COOH. For the directly attached phosphonic acid group (Pe'-$PO(OH)_2$) this effect is less pronounced and the Franck-Condon progression is still observable in the absorption spectrum of the adsorbed molecule. This is in agreement with a longer injection time of 28 fs for Pe'-$PO(OH)_2$ compared to Pe'-COOH when measured with transient cation absorption spectroscopy [64]. Injection times for the above mentioned

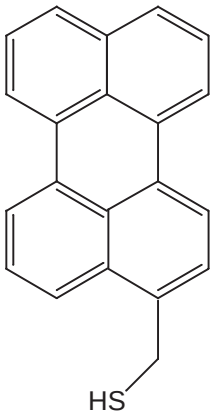

Figure 2.13: Structural formula of Pe-CH-2-S.

molecules with the exception of the Pe'-rod as determined by transient absorption spectroscopy have been reported in Ref. [64]. The knowledge of the lifetimes of the different molecules turned out to be valuable information for interpreting the transient signals measured via TR-2PPE in this work. A comparison of results obtained with the two different experimental techniques will be given in Sec. 4.
In addition, measurements were carried with a perylene chromophore attached to a silver single crystal surface. For this purpose a thiolate group was attached to function as the anchor group. A Pe'-thiol derivative containing the bulky side groups was not at hand. The structure of Pe-CH_2-SH is shown in Fig. 2.13.

2.6.2 The substrates

2.6.2.1 Titanium dioxide

Three crystallographic structures of TiO_2 are found in nature: rutile, anatase and brookite. Others are known but of minor importance. The rutile structure is the most stable one in terms of thermodynamics. Macroscopic single crystals can be grown in the laboratories. At high temperatures ($\sim$ 775 °C), anatase makes a phase transition to rutile and hitherto macroscopic single crystals can only be grown with a high doping level for stabilization. Nevertheless, anatase can be efficiently grown in the form of colloids and is widely used in science and technology. Colloidal films of anatase exhibit a sponge like structure resulting in a surface enhancement of about a factor of 100 for a thickness of 1 μm. This property is used in the dye sensitized solar cell and makes such systems accessible to stationary and transient optical spectroscopy where, until now, sensitivity is insufficient to measure sub monolayer coverages on atomically flat surfaces. The brookite phase is stable only at low temperatures and of minor importance with respect to science and technology.

TiO_2 rutile bulk structure The bulk structure (Fig. 2.14) of rutile is tetragonal with symmetry $D_{4h}^{14} - P4_2/mnm$ and lattice parameters a=b=4.584 Å, c=2.953 Å. The titanium atoms are six- and the oxygen atoms are three-fold coordinated.
Rutile exhibits a band gap of 3.03 eV. The lower conduction bands have a high effective mass. Thus, it is not clear whether the gap is direct or indirect. Arguments for both versions exist: a dipole-forbidden direct gap [68] or an indirect gap [69]. Fig. 2.15 shows the bulk band structure of rutile TiO_2.

An important issue for experimentalists are bulk defects which lead to n-doping by oxygen deficiencies and hence ensure a sufficient conductivity for electron spectroscopy, electron diffraction and scanning tunneling spectroscopy. Various kinds of defects have been reported for different treatments and oxygen deficiencies. In Ref. [70] it is reported that for the range of $3 * 10^{18}$ to $1 * 10^{19}$ missing O atoms per cm^2 titanium interstitials are the dominant defects. Bulk defects give rise to a color change of the crystal ranging from transparent for the undoped nonconducting crystal to dark blue for heavily reduced crystals.

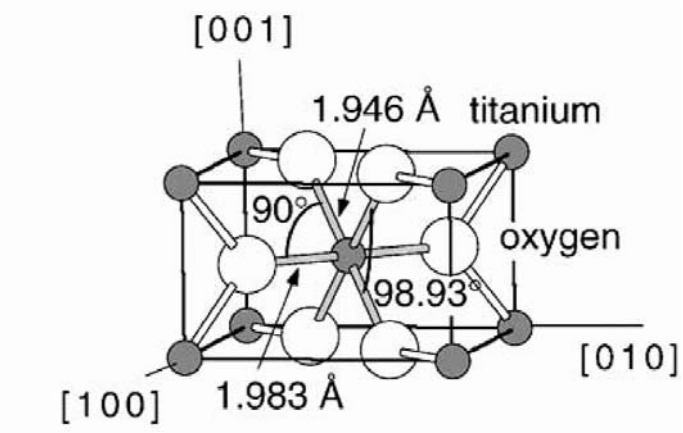

Figure 2.14: Rutile bulk structure from Ref. [2]

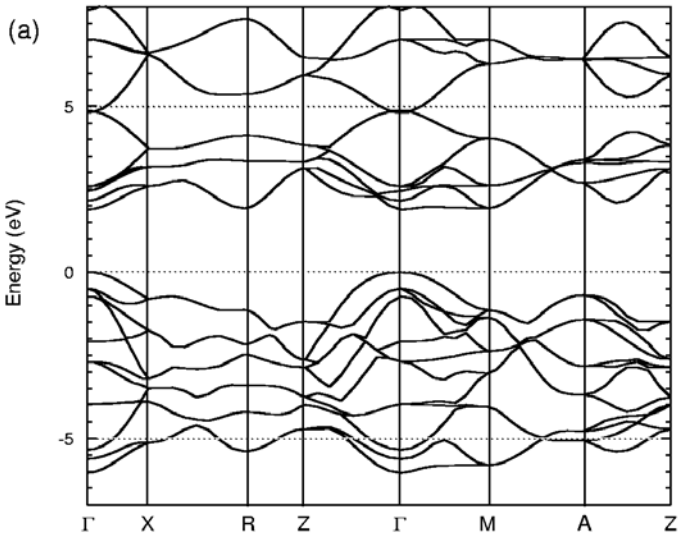

Figure 2.15: Rutile bulk band structure from Ref. [3]

TiO_2 **rutile (110) surface** The (110) surface (Fig. 2.16) is the most stable surface of rutile with the lowest surface energy. It is the stoichiometric, unreconstructed surface. It exhibits the same amount of cation- and anion-derived dangling bonds such that autocompensation via filling (depletion) of anion (cation)-derived dangling bonds stabilizes the surface (LaFemina in Ref. [71]). The (110) surface is composed of five- and six-fold coordinated titanium, and three- and two-fold coordinated oxygen.

The (110) surface is easy to prepare by means of standard vacuum techniques. This may be one reason why it is extensively studied. Another reason is the wide range of technical applications e.g. as a (photo)catalyst, in gas sensors, in electric

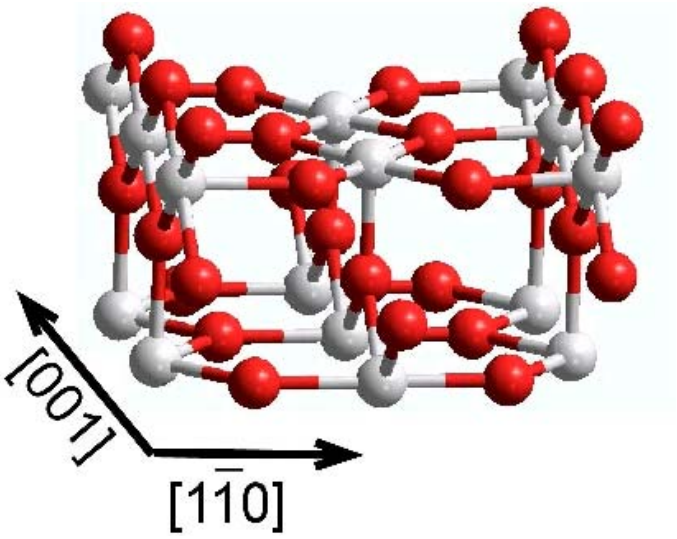

Figure 2.16: The rutile (110) surface structure.

devices and in dye sensitized solar cells. The TiO_2(110) surface has become the model system for metal oxide semiconductor surfaces hence there are numerous reviews [2, 72]. A great variety of experimental techniques has been applied to it as well as theoretical calculations on bulk- and surface-structure, electronic structure [6] and optical properties [7] were performed on it.

Cleaving the surface is hardly possible and the preparation of the (110) surface is commonly done by Ar^+ ion bombardment and annealing the mechanically polished crystal. Additionally, bulk defects are introduced during annealing, which provide reasonable conductivity for electron spectroscopy and STM.

It has been known for long that the surface of rutile is losing oxygen due to ion bombardment and partially restored by vacuum annealing [82]. Nonetheless, a vivid discussion of the reaction mechanisms and the reoxidation dynamics is still going on [83, 84, 85, 86]:

SSIMS measurements on isotopically labeled TiO_2 samples by Henderson et al. have shown, that the diffusing species in the annealing process is titanium and not, as has been assumed previously, oxygen vacancies [87, 88]. When a surface reduced TiO_2 crystal is heated in vacuum above 700 K the excess titanium at the surface diffuses into the bulk occupying interstitial sites.

It is a common preparation procedure to heat such pretreated crystals in an oxygen atmosphere of 10^{-8} to 10^{-6} mbar to reduce surface oxygen vacancies. This treatment leads to a growth of the surface by oxidizing Ti bulk interstitials that are diffusing back to the surface. The growth kinetics depend strongly on temper-

[6] see [73, 74, 3, 75, 76, 77, 78, 79]
[7] see [80, 81, 74]

ature, oxygen pressure and the "history" of the sample. This has been observed by Smith et al. [89] via time-resolved STM imaging during reoxidation of reduced TiO_2 in oxygen, and by McCarty et al. [86], who observed a temperature-driven net flux of Ti and O between surface and bulk via LEEM.
Heating in vacuum at high temperatures, electron- and ion-bombardment all lead to a decrease of the oxygen concentration on the surface. This can be seen:

- in XPS measurements by a formation of a Ti^{3+} peak [90, 91]
- in UPS by the formation of an occupied gap state 0.7 eV below the conduction band minimum,
- in LEED patterns as a 1x2 reconstruction,
- or more directly as bright spots in STM images.

Moderate heating of such reduced samples even in vacuum "heals" the defects via the above described annealing process. The latter process is of course thermodynamically limited. Surfaces that are free of defects are not expected.
STM seems to be the most reliable method to determine the oxygen defect concentration at the surface. In Ref. [2] a defect density of $\sim 7\%$ is reported for an Ar^+ ion bombarded surface heated at 1100 K in vacuum for 10 min. This preparation procedure is comparable to the one used in this work. XPS and UPS seem to be not sensitive enough to detect such defect concentrations, since no noticeable differences in UPS, Auger and IPES signals have been reported, between samples annealed in vacuum and in the presence of oxygen [92, 93].
Many authors have published preparation recipes involving annealing of the sputtered surface in oxygen atmosphere [90, 85, 94, 95]. A comprehensive study of reoxidation at TiO_2(110) surfaces during heating (500-830 K) in an oxygen atmosphere ($1*10^{-7}$-$1*10^{-6}$ mbar) has shown oxygen-induced restructuring effects, like strands, rosettes and terraces, in STM [96]. Above 850 K the surface showed large (1x1) terraces similar to UHV-annealed samples.
Onda et al. claimed that the defect concentration is directly related to the work function of the sample in that a higher work function indicates a lower defect concentration [85]. On the other hand, Diebold et al. have reported that a heavily reduced crystal exhibits a higher work function than less reduced samples [72]. Other reported values for the work function of the (110) surface are ranging from 4.4 up to 5.8 eV and even higher ([97] and references herein, [98, 99, 100]), thus the work function may not be appropriate for a surface quality check (see Sec. 4.1.1).

The above information at hand, the author decided to prepare the rutile (110) surface with Ar^+ ion bombardment (700 eV) followed by moderately heating the sample in vacuum (875 K). In addition, samples were prepared by heating in oxygen atmosphere and no differences to the vacuum annealed samples could be detected neither with UPS nor with TR-2PPE. A detailed characterization of the prepared samples will be discussed in Sec. 3.4.2.

Methanol and toluene on TiO_2 Since dye molecules were dissolved in a mixture of toluene and methanol, possible coadsorption of solvent molecules should be kept in mind. Recent studies have shown molecular adsorption of methanol on $TiO_2(110)$ below room temperature. Henderson et al. have reported that the majority of the methanol adlayer adsorbs molecularly and desorbs at 295 K, dissociatively adsorbed methanol at five-fold coordinated Ti atoms desorbs at 350 K and dissociatively adsorbed methanol at oxygen vacancies at 480 K [101]. Measurements showed that the samples used in this work were heated to about 360 K by illumination with a halogen lamp used for sample alignment. Thus, only methanol adsorbed at vacancy sites was potentially present.
To my knowledge, for toluene no data are available. TDS for benzene shows molecular desorption at 260 K [102] and it is highly likely that even toluene desorbs below room temperature as it is bound only trough weak Van-der-Waals interactions.

Carboxylic acids on TiO_2 Formic acid may be the most frequently investigated organic adsorbate on TiO_2. A review and a summary of citations are given in Ref. [2]. It is reported that formic acid adsorbs dissociatively on TiO_2 surfaces at room temperature as formate plus hydroxyl [103].

$$HCOOH + O^{-2}_{surface} -> HCOO^{-}_{adsorbed} + OH^{-}_{adsorbed} \tag{2.6.1}$$

Where $O^{-2}{}_{surface}$ is the surface bridging oxygen. On (110) rutile surfaces formate bonds to two five fold coordinated Ti atoms in a bridging geometry resulting in a p(2x1) LEED pattern [104]. Whereas this binding geometry is supported by many experiments of the adsorption of formic acid from the gas phase by preparation in UHV, calculations for different conformations revealed that even an ester-like binding has a slightly higher binding energy than molecular methanol (Fig. 2.17). The ester binding is reported for the rutile (111) surfaces and is attributed to

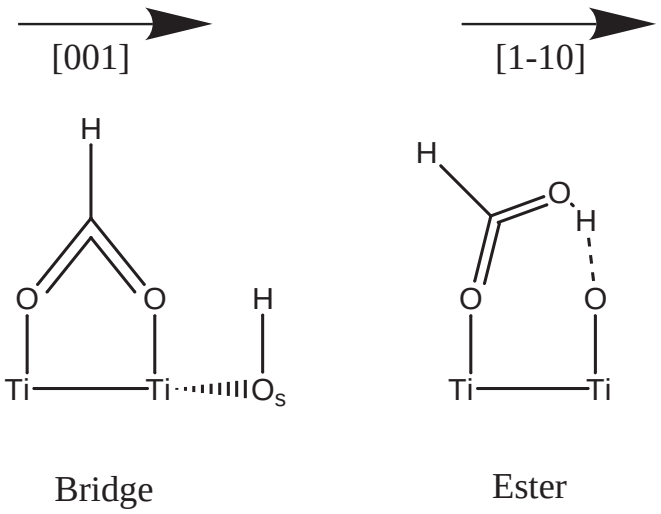

Figure 2.17: Binding conformations of formate on TiO_2(110). a) bidentate binding, b) ester binding.

the Ti-Ti distance being larger than on the rutile (110) surfaces [105] and for carboxylic acid on anatase surfaces [106]. The ester binding may also occur on rutile (110) surfaces when formic acid is adsorbed in competition with methanol. Benzoic acid is reported to adsorb in the bridge bonding conformation [107, 108]. The phenyl rings are perpendicular to the surface and arranged in rows with the molecular plane perpendicular to each other.

Phosphonic acids on TiO_2 Phosphonic acid has been reported to bind more strongly to TiO_2 than carboxylic acid. Pawsey et al. studied the adsorption of carboxy-alkyl-phosphonic acids on colloidal TiO_2. They have reported that these molecules bind with the phosphonic acid group to TiO_2 rather than with the carboxylic acid group [109].
Furthermore, Nilsing et al. performed DFT calculations to study the binding geometry of phosphonic acid on anatase (101) surfaces [110]. They have calculated the adsorption of phosphonic acid significantly stronger than that of formic acid. The strongest adsorption of phosphonic acid on anatase TiO_2(101) has been reported to be a monodentate geometry with two hydrogen bonds and one metal:oxygen bond.
On the other hand, Guerrero et al. have reported a tridentate bonding geometry for phosphonic acid on anatase colloids, as deduced from NMR and IR spectroscopic investigations [111].
Similar results for the adsorption of phosphonic acid on rutile (110) surfaces have not been reported to the best of my knowledge. Phosphonic acid can

bind via three oxygen atoms in a triangular conformation, but considering the surface structure of $TiO_2(110)$ the five-coordinated Ti^{4+} atoms are arranged in rows unless an oxygen vacancy is present. Since the density of oxygen vacancies is believed to be around 7% a mono- or bidentate bonding geometry is expected for the adsorption of phosphonic acid on the rutile (110) surface of TiO_2.

2.6.2.2 Copper and silver

The low index surfaces of noble metals are among the best investigated surfaces as far as TR-2PPE is concerned. In particular, image potential states proposed by Echenique et al. [112] 30 years ago have attracted considerable attention because of their special properties. Image potential states at metal surfaces have been studied extensively ([25, 46] and references herein). Many low-index surfaces of noble-metals exhibit a surface-projected bandgap at $\bar{\Gamma}$. An electron in front of such a surface is trapped by the induced image potential on one side and the bandgap on the other side. The resulting potential generates a Rydberg-like series of bound states in the surface normal direction. These states can be optically populated from the occupied surface state (SS) either resonantly or off-resonantly by quasi-elastic scattering [113].
The main decay channel for the excited image potential state (IS) is governed by the overlap of the IS with the bulk [114]. The decay of hot bulk electrons in noble metals especially in copper and gold have been discussed extensively due to the anomalous long lifetimes of hot electrons with little excess energy. This anomaly is ascribed to Auger excitation of d-band electrons [50, 36, 34]. This effect is prominent in copper and gold because the d-bands in both metals are located about 2 eV below the Fermi level and direct optical excitation from occupied d-band states to unoccupied sp-band states is the dominant absorption process for photon energies above 2 eV resulting in hot d-band holes. For silver the d-bands are located 4 eV below the Fermi level and thus direct interband excitation is not accessible with the pump photon energy used in this work. Ag(111),(110) and Cu(111) surfaces were investigated in this work for two reasons. First, they are excellent samples to test the TR-2PPE apparatus and compare the data with published results because of the large number of published experiments and the narrow spectral features (i.e. image potential states). Secondly, the silver surfaces were used to gain insight into the contribution of the substrate to the 2PPE signal in substrate-adsorbate systems. In contrast to the Cu and Ag(111) surfaces the Ag(110) surface has no surface projected band-gap at the Γ-point.

Thus, image potential states at this surface are resonant with bulk states resulting in a strong reduction in the lifetime and thus much lower emission yield of 2PPE. Together with the weak signal originating from indirect sp-intraband transitions this surface is well suited for the investigation of adsorbate states. From previous 2PPE studies lifetime of 18±5 fs was deduced for the n=1 IS on Cu(111) [113]. TR-2PPE studies by Schoenlein et al. indicate lifetimes of less then 20 fs for the n=1 and n=2 image potential state of Ag(111), respectively [115]. More recently, Lingle et al. have reported 32±10 fs and sub-20 fs for the n=1 and n=2 image potential state of the same system, respectively [116].